ACS APPLIED MATERIALS & INTERFACES

Research Article

www.acsami.org

Nanocrystal-Constructed Mesoporous Single-Crystalline Co_3O_4 Nanobelts with Superior Rate Capability for Advanced Lithium-Ion Batteries

Hui Huang, Wenjun Zhu, Xinyong Tao, Yang Xia, Zhaoyang Yu, Junwu Fang, Yongping Gan, and Wenkui Zhang*

College of Chemical Engineering and Materials Science, Zhejiang University of Technology, Hangzhou 310014, China

Supporting Information

ABSTRACT: In this paper, one-dimensional (1D) mesoporous single-crystalline Co_3O_4 nanobelts are synthesized by a facile hydrothermal method followed by calcination treatment. The as-prepared nanobelts have unique mesoporous structures, which are constructed by many interconnected nanocrystals with sizes of about 20−30 nm. And typical size of the nanobelts is in the range of 100−300 nm in width and up to several micrometers in length. The BET surface area of Co_3O_4 nanobelts is determined to be about 36.5 m^2 g^{-1} with dominant pore diameter of 29.2 nm. Because of the 1D structure, mesoporous morphologies and scrupulous nanoarchitectures, the Co_3O_4 nanobelts show excellent electrochemical performances such as high storage capacity and superior rate capability. The specific capacity of Co_3O_4 nanobelts could remains over 614 mA h g^{-1} at a current density of 1 A g^{-1} after 60 cycles. Even at a high current density of 3 A g^{-1}, these Co_3O_4 nanobelts still could deliver a remarkable discharge capacity of 605 mA h g^{-1} with good cycling stability.

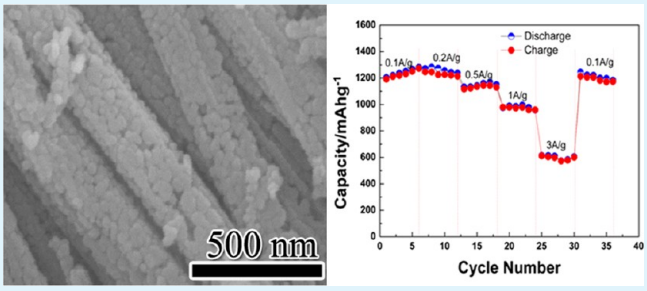

KEYWORDS: *Co_3O_4, hydrothermal synthesis, mesoporous nanobelts, single-crystalline, lithium-ion batteries*

1. INTRODUCTION

Rechargeable lithium-ion batteries (LIBs) have attracted considerable interest as one of the most promising energy storage devices.[1−3] Nowadays, a major challenge for LIBs is to develop new materials with high energy density, long cycle life, and excellent rate capability for practical applications in high-power electric vehicles and portable electronic devices. Recently, transition metal oxide (e.g., Co_3O_4) has received increasing attention as a promising alternative anode material to graphite on the basis of its higher theoretical capacity (892 mAh g^{-1} for Co_3O_4).[4−6] However, despite its ultrahigh capacity, the practical application of Co_3O_4 is still largely restrained by the slow kinetics of Li-ion and electron transport in electrodes and at the interface of electrode/electrolyte, poor capacity retention resulting from the large volume changes over extended cycling.[7,8]

To circumvent the above drawback, great efforts have been devoted to designing effective micro/nanostructures of Co_3O_4 to optimize and enhance electrochemical performance. To date, various Co_3O_4 micro/nanostructures including one-dimensional (1D) nanowires,[9,10] nanobelts,[11−14] nanorods,[15,16] nanoneedles[17,18] and nanotubes,[19,20] two-dimensional (2D) nanosheets,[21,22] three-dimensional (3D) architectures,[23] nanoparticles,[4,24] and nanocubes[25,26] have been prepared by a rich variety of methods and mechanisms, e.g., template-assisted synthesis, precursor conversion processes, sol−gel, thermal decomposition, solvothermal and hydrothermal methods, microemulsion-based routes, etc.[16,27−31] Moreover, it is found that the electrochemical performance of Co_3O_4 electrodes strongly depends on the morphology and the porosity of the structure. Lee et al.[32] reported a cryogel synthesis of ultrafine Co_3O_4 nanocrystals with in situ construction of mesoporous/macroporous networks for supercapacitor electrode material. Kim et al.[33] synthesized porous Co_3O_4 hollow rods using bacteria as a soft template, presenting enhanced electrochemical properties. Among the reported Co_3O_4 nanostructures, 1D Co_3O_4 nanomaterials are expected to have high performance in energy storage systems because it facilitates the electron transport along the long dimension and the two short dimensions ensure fast Li^+ insertion/extraction. Wu et al.[9] reported that a Li^+ ions intercalation capacity of over 700 mA h g^{-1} for mesoporous Co_3O_4 nanowire arrays prepared by ammonia-evaporation-induced method can be obtained. Zhu et al.[16] also reported that porous rhombus-shaped Co_3O_4 nanorod arrays grown directly on a nickel substrate exhibited a high reversible capacity (over 1000 mA h g^{-1}). However, the long-term cycling stability and high rate performances of these 1D nanostructures are still far from satisfactory. Recent researches

Received: August 13, 2012
Accepted: October 10, 2012
Published: October 10, 2012

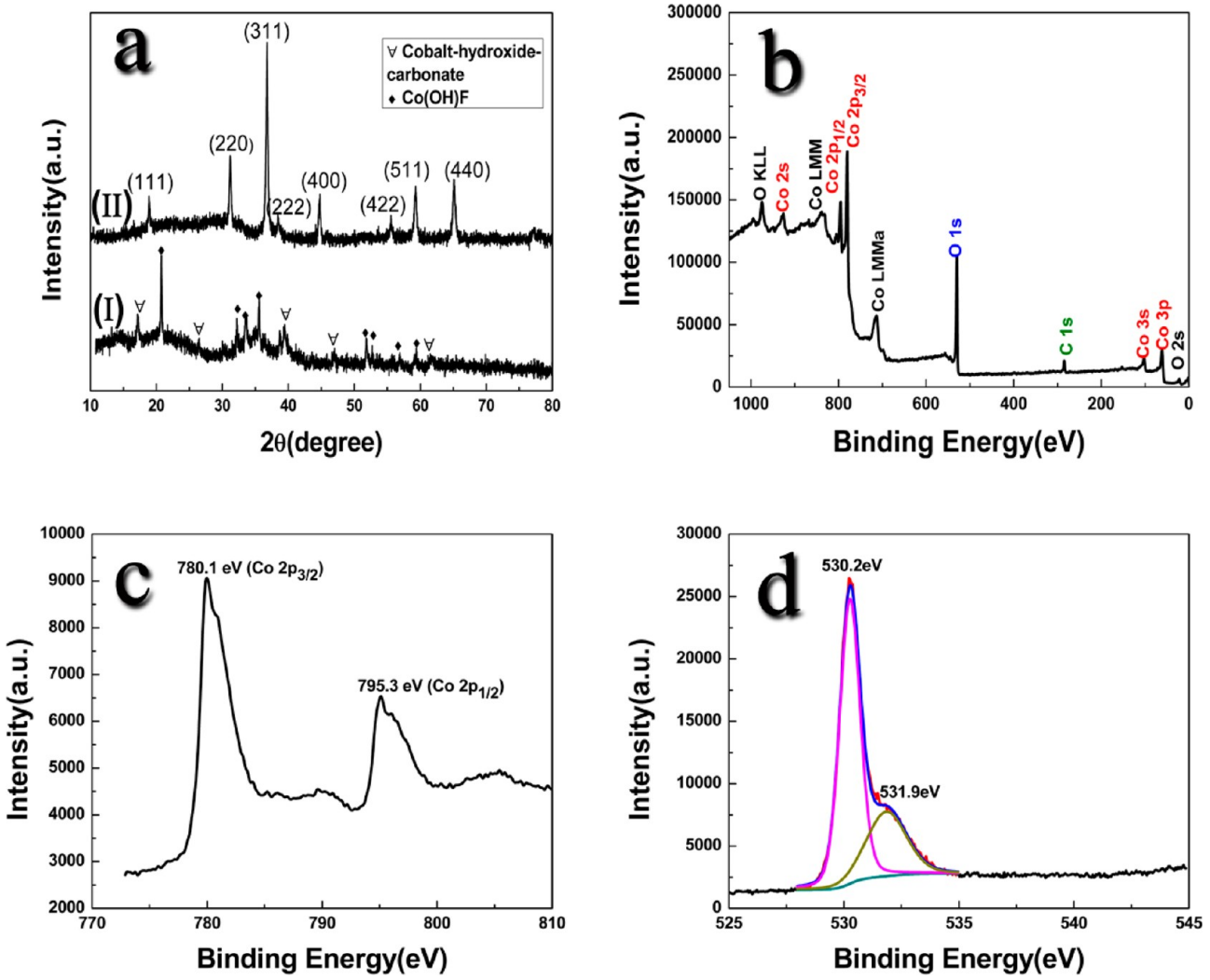

Figure 1. (a) XRD patterns of (I) the precursor and (II) Co_3O_4; (b–d) XPS spectrum of Co_3O_4: (b) full survey scan spectrum, (c) Co 2p, and (d) O1s peak.

have demonstrated that 1D porous morphology could guarantee high electrode/electrolyte contact area, accommodate the volume changes resulting from repeated charge/discharge cycling, and thus avoiding the rapid capacity fading especially at high rates.[9,25,33−36] Lou et al.[19] revealed that mesoporous Co_3O_4 nanoneedles with a 3D single-crystalline framework, based on thermal decomposition and recrystallization of β-$Co(OH)_2$ nanoneedle precursor, delivered ultrahigh capacity, and excellent cycling performance. Considering the merits of 1D single-crystalline materials, such as well-defined geometry and perfect crystallization, 1D single-crystalline mesoporous Co_3O_4 nanobelts will be very attractive as anode materials for advanced LIBs. However, up to now, there are few reports about 1D single−crystalline mesoporous Co_3O_4 nanobelts for advanced LIBs. In the present work, we develop a facile way to synthesis 1D single−crystalline mesoporous Co_3O_4 nanobelts without any template or structure−directing agent. It involves the synthesis of 1D precursor compounds through hydrothermal synthesis followed by calcination to form scrupulous nanocrystals−constructed mesoporous Co_3O_4 nanobelts. For its high porosity, single-crystalline and hierarchically structure, it could exhibits ultrahigh reversible capacity, and excellent capacity retention and superior rate performances.

2. EXPERIMENTAL SECTION

Materials Synthesis. All chemicals were of analytical grade and used as received without further purification. In a typical synthesis of the cobalt precursor, 5 mmol of $Co(NO_3)_2{\cdot}6H_2O$, 10 mmol of NH_4F, and 25 mmol of $CO(NH_2)_2$ were dissolved in 50 mL of deionized water under stirring for 10 min at room temperature. Then the solution was transferred into a Teflon-coated stainless steel autoclave at 120 °C for 24 h. After being cooled down to ambient temperature, the pink cobalt precursor was filtered and thoroughly washed with deionized water several times to neutral. Afterward, pure spinel Co_3O_4 phase was obtained by calcination of the precursor at 400 °C for 4 h in air.

Structure Characterizations. The as-prepared products were characterized using powder X-ray diffractometry (XRD; X'Pert Pro diffractometer with a Cu Kα radiation, λ = 0.15418 nm), scanning electron microscopy (SEM; Hitachi S-4700) and transmission electron microscopy (TEM; FEI, Tecnai G2 F30. JEM-2100 and JEM-2100F), equipped with an energy dispersive spectroscopy (EDS) detector. X-ray photoelectron spectroscopy (XPS) measurements were performed on a Thermo ESCALAB 250 system with a monochromatic Al−Kα (1486.6 eV) X-ray source. The thermal decomposition behavior of the precursors was examined by thermogravimetric analysis and differential scanning calorimetry (TG/DSC, STA449) at a heating rate of 5 °C min^{-1} from room temperature (25 °C) to 700 °C in air flow. Nitrogen adsorption/desorption was determined by Brunauer−

Emmett–Teller (BET) tests using an ASAP 2020 (Micromeritics Instruments) surface area and pore analyzer.

Electrochemical Measurements. Electrochemical experiments were carried out using standard CR 2025 type coin cells. The as-prepared Co_3O_4 sample was mixed with acetylene black and polyvinylidene fluoride (PVDF) binder at a weight ratio of 75:15:10 in N-methyl-2-pyrrolidene (NMP) solution. The slurry was pasted on a Cu foil and dried in a vacuum oven at 120 °C for 12 h to serve as the working electrode. The weight of the active material in the electrode sheet was about 5 mg/cm^2. A pure lithium foil was used as both counter electrode and reference electrode. A solution of 1 M $LiPF_6$ in ethylene carbonate (EC)/dimethyl carbonate (DME) (1:1 by volume) was used as the electrolyte, and a polypropylene microporous film (Cellgard 2300) as the separator. Galvanostatical charge–discharge experiments were tested at different current densities in a voltage range of 0–3.0 V on a battery test system (Shenzhen Neware Battery, China). Cyclic voltammetry (CV) measurements were carried out on a CHI650B electrochemical workstation (Shanghai Chenhua, China). The CVs were obtained over the potential range of 0–3.0 V at a scanning rate of 0.1 mV s^{-1}.

3. RESULTS AND DISCUSSION

The synthesis includes two crucial steps, formation of precursor *via* a hydrothermal process and subsequent thermal conversion to Co_3O_4. It is clear from pattern I in Figure 1a that the pink precursor contains mixed phases of Co(OH)F (JCPDS No. 50–0827) and cobalt-hydroxide-carbonate (JCPDS No. 38–0547). The formation of Co(OH)F precursor was also verified by the EDS analysis (see the Supporting Information, Figure S1), which reveals the existence of F element in the sample. Pattern II in Figure 1a reveals that all the diffraction peaks can be indexed to cubic spinel Co_3O_4 (JCPDS No. 43–1003, space group: *Fd*3*m*, lattice constant a = 8.08 Å). No other peaks of impurities are observed, indicating that the cobalt precursor was converted to crystalline Co_3O_4 completely. Jiang et al.[37] reported that the as-synthesized precursor is composed of cobalt–hydroxide–carbonate, whereas this work indicated the presence of two precursors of Co(OH)F and cobalt–hydroxide–carbonate.

Further surface information on the purity and composition of the Co_3O_4 sample was collected *via* X-ray photoelectron spectroscopy (XPS). The binding energies obtained in the XPS analysis were calibrated for specimen charging by referencing the C1s peak to 284.80 eV. As shown in Figure 1b, the sharp peaks at 284.8, 531.4, and 782.6 eV correspond to the characteristic peaks of C 1s, O 1s, and Co 2p, respectively, indicating the existence of carbon, oxygen, and cobalt elements in the sample. The Co 2p peaks at 795.3 and 780.1 eV can be attributed to Co $2p_{1/2}$ and Co $2p_{3/2}$ of Co_3O_4,[38] with a spin-orbit splitting of 15.2 eV (Figure 1c). The absence of prominent shakeup satellite peaks in the Co 2p spectra further suggests the formation of the Co_3O_4 phase. The deconvoluted O 1s spectrum in Figure 1d displays two peaks at 530.2 and 531.9 eV, which can be assigned to the lattice oxygen of spinel Co_3O_4, the oxygen in hydroxide ions, respectively.[39] The XPS results further confirm that the as-synthesized product is pure cobalt oxide.

On the basis of these results and previous reports, we propose a possible formation mechanism of mixed precursors. At the beginning of the hydrothermal reactions, Co^{2+} ions can coordinate with F^- ion to form CoF^+ and $CoF_x^{(x-2)-}$ complexes in the homogeneous solution. With the temperature of the reactant solution increasing to 120 °C, the hydrolysis–precipitation process of urea took place and a number of CO_3^{2-} and OH^- anions were formed gradually, which could help to release Co^{2+} ions slowly from complexes. As a result, OH^- can reacts with CoF^+ to form Co(OH)F crystals. At the same time, CO_3^{2-} reacts with OH^- and $CoF_x^{(x-2)-}$ to form cobalt–hydroxide–carbonate. The involved chemical reactions may occur as the following formulas 1–6[16,37]

$$Co^{2+} + F^- \rightarrow CoF^+,\ Co^{2+} + xF^- \rightarrow CoF_x^{(x-2)-} \quad (1)$$

$$H_2NCONH_2 + H_2O \rightarrow 2NH_3 + CO_2 \quad (2)$$

$$CO_2 + H_2O \rightarrow CO_3^{2-} + 2H^+ \quad (3)$$

$$NH_3 + H_2O \rightarrow NH_4^+ + OH^- \quad (4)$$

$$CoF^+ + OH^- \rightarrow CoF(OH) \quad (5)$$

$$CoF_x^{(x-2)-} + 0.5(2-y)CO_3^{2-} + yOH^- + nH_2O \rightarrow Co(OH)_y(CO_3)_{0.5(2-y)}\cdot nH_2O + xF^- \quad (6)$$

The thermal decomposition behavior of the mixed precursors was examined by thermogravimetric analysis and differential scanning calorimetry. As shown in Figure 2, the initial weight

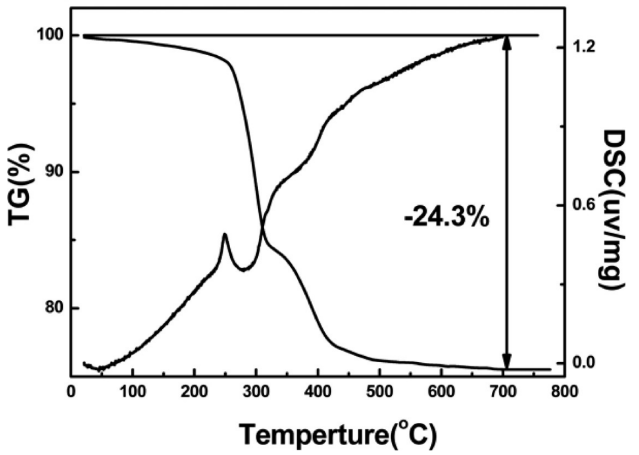

Figure 2. TG-DSC curves of the precursors in air with a heating rate of 5 °C min^{-1}.

loss of about 2% up to 250 °C is mainly due to the elimination of absorbed/trapped water. Subsequently, there is a distinct weight loss of about 22% occurred from 250 to 500 °C and an obvious exothermic process is observed in the DSC curve. This stage is mainly associated with the decomposition of the two precursors and thermal formation of Co_3O_4 product, as demonstrated in the formulas 7 and 8.

$$6CoF(OH) + O_2 \rightarrow 2Co_3O_4 + 6HF \quad (7)$$

$$3Co(OH)_y(CO_3)_{0.5(2-y)}\cdot nH_2O + 0.5O_2 \rightarrow Co_3O_4 + (3n + 1.5y)H_2O + 1.5(2-y)CO_2 \quad (8)$$

Figure 3 presents low- and high-magnifcation SEM images of the as-prepared precursor and Co_3O_4 nanobelts. It is observed from Figure 3a and b that the precursor consists of uniform 1D nanobeltlike structures, and their typical size is in the range of 2–3 um in length and 100–300 nm in width. Figure 3c shows that the nanobelt structure of the final product after calcination does not change much. The diameter and length of Co_3O_4 nanobelts are similar to those of the precursor, but the surfaces

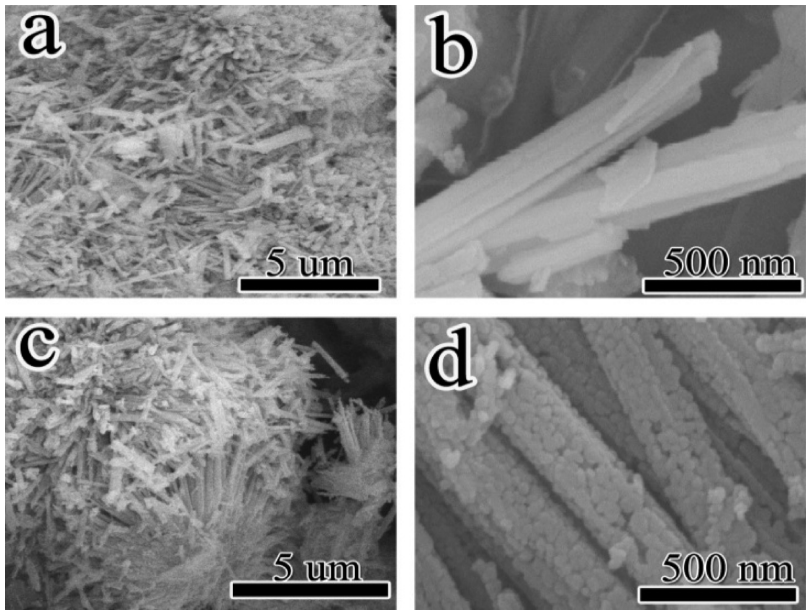

Figure 3. Typical low-magnification and high-magnifcation SEM images of as-prepared (a, b) precursor and (c, d) Co_3O_4 nanobelts.

of these nanobelts are extraordinary rough. The high-magnification SEM image in Figure 3d further reveals that these nanobelts are an assembly of many fine nanocrystals, forming a large quality of interconnected mesoporous structures on the surfaces of Co_3O_4 nanobelts. This could be ascribed to the successive release and loss of CO_2, HF, and H_2O during the thermal decomposition of precursors.

The microstructure of the Co_3O_4 nanobelts was further investigated by TEM and HRTEM. TEM images a and b in Figure 4 show that the Co_3O_4 nanobelts are constructed from numerous nanocrystals with a size in the range of 20−30 nm. An individual Co_3O_4 nanobelt has a diameter of 150 nm with small intercrystallite pores and rough surfaces, which agrees with SEM observations. The distinct lattice stripes in the HRTEM image (Figure 4c) reveal the Co_3O_4 nanobelt is well crystallized. Figure 4d−f presents the magnified HRTEM images of different regions marked in Figure 4c and corresponding FFT images (inset). The lattice spacing of 0.287, 0.467, and 0.244 nm correspond to the (220), (111), (311) crystal planes of spinel Co_3O_4, respectively, in good agreement with the original XRD pattern in Figure 1a (II). The FFT patterns of the three different regions all show the same grain orientation, which further confirm a high crystallinity of the mesoporous single-crystal nature Co_3O_4 nanobelts.

Nitrogen isothermal absorption−desorption measurements were performed to determine the Brunauer−Emmett−Teller (BET) surface area and the porosity of the mesoporous Co_3O_4 nanobelts. Figure 5 shows the isotherm curve, which is a typical type IV with a hysteresis loop at relative pressure of 0.76−1.0, representing the mesoporous structure.[3] The BET specific surface area of the mesoporous Co_3O_4 nanobelts is calculated to about 36.5 $m^2\ g^{-1}$. The pore size distribution curve in the inset of Figure 5 suggests most pores are around 29.2 nm, in good agreement with the TEM results.

Figure 6a shows the initial three charge−discharge profiles at a current density of 50 mA g^{-1} in the voltage range of 0−3.0 V. During the first charge−discharge processes, the Co_3O_4 electrode delivers an initial discharge capacity of 1412 mAh g^{-1} and charge capacity of 1269 mAh g^{-1} with a high columbic efficiency of 89.8%, which is much higher than those recently reported by others.[16,19,40−42] Generally, the mechanism of Li ion storage for oxide materials during the first discharge process includes two types. One is the electrolyte decomposition and inevitable formation of a solid electrolyte interphase (SEI), which is partially irreversible, and the second is a reversible redox reaction mechanism, which has been previously reported in the literature.[11,43]

$$Co_3O_4 + 8Li^+ + 8e^- \leftrightarrow 4Li_2O + 3Co \quad (9)$$

It is known that the irreversible capacity is associated with the specific surface area of materials. The large specific surface area may results in a high irreversible capacity in the first cycle. Interestingly, we note that the investigated Co_3O_4 nanobelts possess a specific surface area of 36.5 $m^2\ g^{-1}$, which is comparable with most of other Co_3O_4 nanostructures reported previously,[17,39] but the irreversible capacity loss is very low (only about 10.2%). The results suggest that the irreversible capacity loss of the Co_3O_4 nanobelts is associated more directly with its structural aspects than specific surface area. In the subsequent cycles, the charge−discharge profiles are basically invariable, further confirming the stability and reversibility of the Co_3O_4 anode material for LIBs. The discharge and charge capacities in the third cycle are 1270 mA h g^{-1} and 1216 mA h g^{-1}, respectively. The columbic efficiency of the third cycle is remarkably increased to 95.7%. These results indicate that the Co_3O_4 nanobelts have high charge−discharge reversibility and good cycling stability. Very interestingly, the reversible capacity of Co_3O_4 nanobelts is much larger than the theoretical capacity of bulk Co_3O_4 (892 mA h g^{-1}). These phenomena are commonly observed with transition metal oxide anodes such as CoO_x, FeO_x, MnO_x, etc., which corresponds to the sloping voltage down to ~0 V. Most of this extra capacity could be due to additional lithium storage in the grain boundaries of Li_2O and metal formed in the reduction cycle. For the mesoporous Co_3O_4 nanobelts in this study, there are more mesopores for extra active sites of lithium insertion as well.[16,44] Figure 6b shows the CVs of the Co_3O_4 nanobelts electrode at a scan rate of 0.1 mV s^{-1}. In the first cathodic scan, there is one intense

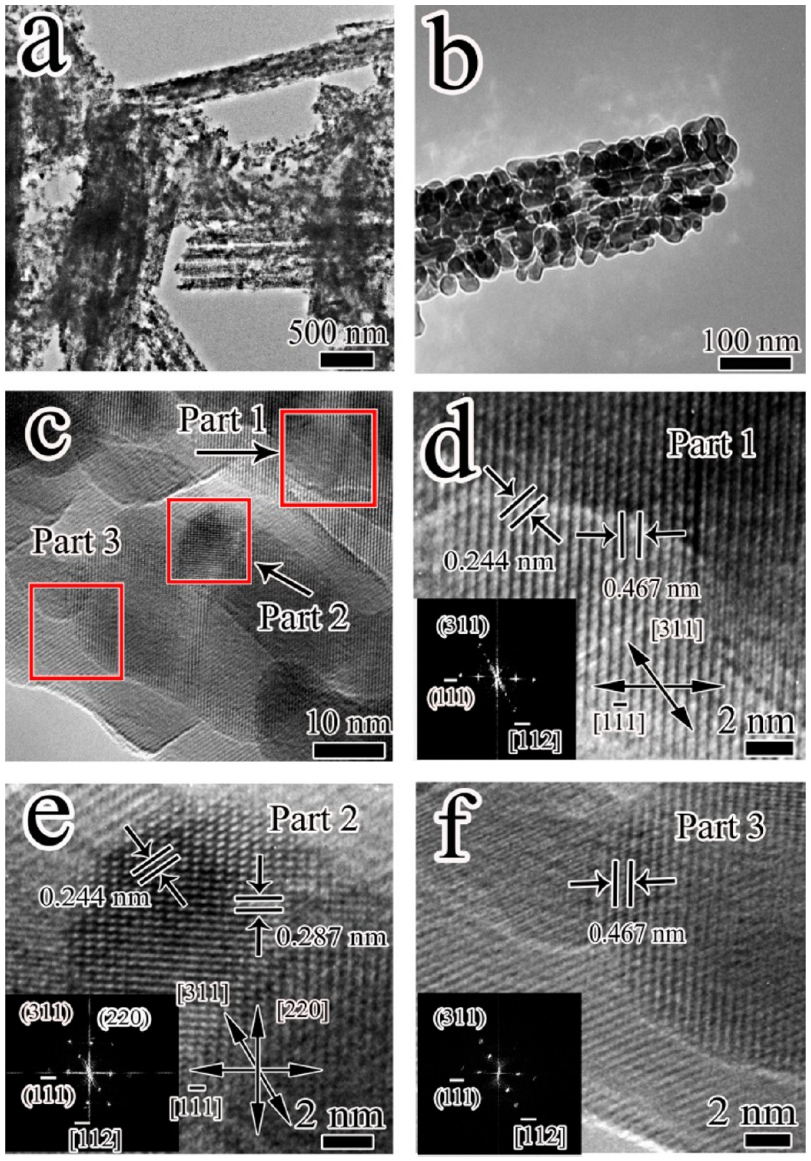

Figure 4. (a, b) Typical TEM images of Co_3O_4 nanobelts. (c) HRTEM image. (d–f) Magnified HRTEM images of the areas indicated by the red rectangle in c and corresponding FFT images (inset).

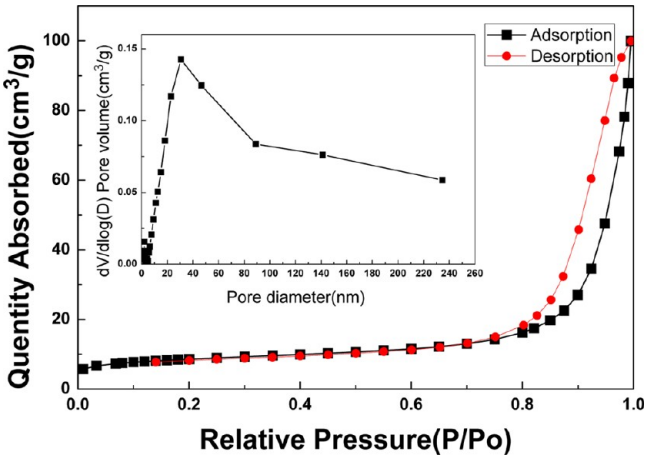

Figure 5. N_2 adsorption–desorption isotherms and pore size distributions curve (inset) of Co_3O_4 nanobelts measured at 77 K.

peak located at around 0.8 V, corresponding to the initial reduction of Co_3O_4 to metallic cobalt accompanying with the electrochemical formation of amorphous Li_2O, and another weak shoulder peak at around 1.1 V, corresponding to the formation of partially irreversible SEI layers.[43] The CV results are consistent well with the two well–defined voltage plateaus in the first discharge profile in Figure 6a. During the subsequent anodic scan, there is a broad peak located at around 2.1 V, which can be ascribed to the oxidation of metallic Co to Co_3O_4 and the decomposition of Li_2O. From the second cycle, the reduction peak is shifted to a higher potential at about 1.2 V while the oxidation peak position is almost unchanged. The subsequent CV curves exhibit good reproducibility and similar shapes, suggesting a high reversibility of lithium storage.

The discharge capacity versus cycle number of the Co_3O_4 electrode in the voltage range of 0–3 V at a current density of 0.1 and 1 A g^{-1} are shown in Figure 6c. The initial discharge capacity of the Co_3O_4 electrode is 1204 mA h g^{-1} at a current density of 0.1 A g^{-1}. Accompanied with the cycle number increasing, the discharge capacity increases in the initial 8 cycles

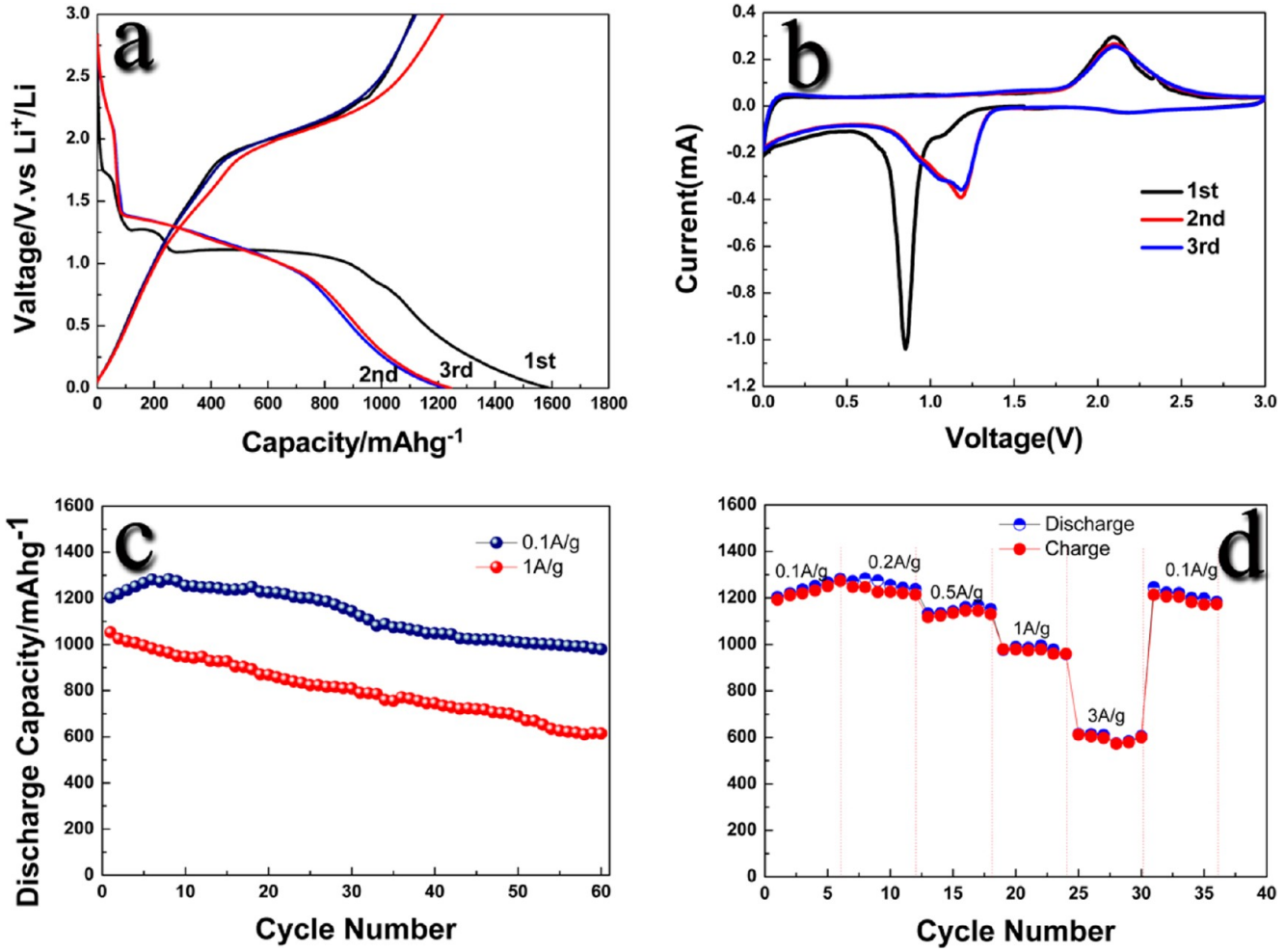

Figure 6. (a) Initial three charge–discharge curves of Co_3O_4 nanobelts at a current density of 50 mA g^{-1}. (b) CVs of Co_3O_4 nanobelts at a scan rate of 0.1 mV s^{-1}. (c) Cycling performance of Co_3O_4 nanobelts at a current density of 0.1 A g^{-1} and 1 A g^{-1}, respectively. (d) Rate performance of Co_3O_4 nanobelts at various current densities.

and then gradually levels off. It can still remains above 980 mA h g^{-1} after 60 cycles. Even at a high rate of 1 A g^{-1}, the electrode also exhibits excellent cycling stability, and the discharge capacity keeps about 614 mA h g^{-1} upon 60 cycles. The cycling performance of the mesoporous Co_3O_4 nanobelts reported here is comparable with those of other 1D mesoporous structures, such as nanoneedles[17] and nanowire arrays.[39] The reason could be that the mesoporous nanostructure of Co_3O_4 nanobelts facilitates the alleviation of the mechanical stress induced by volume change during repeated charge–discharge cycles. Figure 6d compares the rate capabilities (at 0.1 to 3 A g^{-1} rate) of mesoporous Co_3O_4 nanobelts. It can be found that the discharge and charge capacities remain stable and decrease regularly with an increased rate. After each 6 cycles at a specifical current rate, the reversible capacities at 0.1, 0.2, 0.5, 1, and 3 A g^{-1} are about 1282, 1238, 1151, 958, and 605 mA h g^{-1}, implying that the rate cycling stability of the Co_3O_4 nanobelts electrode is excellent. To the best of our knowledge, this is the superior rate performance ever reported as anodes for LIBs among the Co_3O_4 electrodes. It is also noted that the charge and discharge capacities at various rates are nearly the same, indicative of high reversibility. When the current density is decreased from 3 to 0.1 A g^{-1}, the discharge capacity can be recovered (even a little higher than the original capacity at 0.1 A g^{-1}). The results reveal that the mesoporous single-crystalline Co_3O_4 nanobelt electrode has excellent electrochemical reversibility and structural stability.

We believe that the high lithium storage capacity and superior rate capability can be attributed to the unique nanoarchitecture of mesoporous single-crystalline Co_3O_4 nanobelts with a variety of favorable features. First, the ultrahigh reversible capacity (higher than that of the theoretical value) is probably attributable to mesopores, which can accommodate some additional lithium.[44] In addition, nanocrystals could provide more grain boundaries for lithium insertion. Second, the 1D nanostructure of Co_3O_4 ensures fast electron transport and provides short pathways for Li^+ ions insertion/extraction,[16] which is beneficial to enhance the reaction kinetics of Co_3O_4 at different rates. Third, the hierarchically porous structures could enhance the contact area between the electrode and electrolyte, allow better penetration of the electrolyte, and accommodate the large volume changes induced by lithium insertion/extraction, thereby enhancing the rate cycling stability.[9]

4. CONCLUSION

In summary, the 1D mesoporous single-crystalline Co_3O_4 nanobelts have been synthesized by a facile hydrothermal method followed by calcination treatment. The as-synthesized Co_3O_4 nanobelts are constructed by many interconnecting

nanocrystals, exhibiting an interesting mesoporous structure. As a promising anode material for LIBs, the Co_3O_4 nanobelts exhibit high lithium storage capacity, good cycling stability, and superior rate capability. It delivers an initial discharge capacity of 1412.7 mA h g^{-1} at a current density of 50 mA g^{-1}, and maintains high discharge capacities of 980 and 614 mA h g^{-1} at current density of 0.1 and 1 A g^{-1} after 60 cycles, respectively. The cycling reversible capacity still keeps 605 mAh g^{-1} even at a high current density of 3 A g^{-1}. We believe that the unique morphology and scrupulous architecture of the Co_3O_4 nanobelts are responsible for their outstanding electrochemical performances.

■ ASSOCIATED CONTENT

Supporting Information

EDS analysis of the precursor. This material is available free of charge via the Internet at http://pubs.acs.org.

■ AUTHOR INFORMATION

Corresponding Author

*Tel.: +86 571 88320394. Fax: +86 571 88320394. E-mail: msechem@zjut.edu.cn

Notes

The authors declare no competing financial interest.

■ ACKNOWLEDGMENTS

This work was supported by National Natural Science Foundation of China (51172205 and 51002138), Natural Science Foundation of Zhejiang Province (Y4110523), Qianjiang Project of Zhejiang Province (2010R10029), and New Century Excellent Talents in University (NCET 111079).

■ REFERENCES

(1) Arico, A. S.; Bruce, P.; Scrosati, B.; Tarascon, J. M.; Van Schalkwijk, W. *Nat. Mater.* **2005**, *4*, 366.
(2) Tarascon, J. M.; Armand, M. *Nature* **2001**, *414*, 359.
(3) Yan, N.; Hu, L.; Li, Y.; Wang, Y.; Zhong, H.; Hu, X. Y.; Kong, X. K.; Chen, Q. W. *J. Phys. Chem. C* **2012**, *116*, 7227.
(4) Poizot, P.; Laruelle, S.; Grugeon, S.; Dupont, L.; Tarascon, J. M. *Nature* **2000**, *407*, 496.
(5) Poizot, P.; Laruelle, S.; Grugeon, S.; Dupont, L.; Tarascon, J. M. *J. Power Sources* **2001**, *97*−*8*, 235.
(6) Yuan, Z. Y.; Huang, F.; Feng, C. Q.; Sun, J. T.; Zhou, Y. H. *Mater. Chem. Phys.* **2003**, *79*, 1.
(7) Kang, Y. M.; Song, M. S.; Kim, J. H.; Kim, H. S.; Park, M. S.; Lee, J. Y.; Liu, H. K.; Dou, S. X. *Electrochim. Acta* **2005**, *50*, 3667.
(8) Yu, Y.; Chen, C. H.; Shui, J. L.; Xie, S. *Angew .Chem., Int. Ed.* **2005**, *44*, 7085.
(9) Li, Y. G.; Tan, B.; Wu, Y. Y. *Nano Lett.* **2008**, *8*, 265.
(10) Zhang, Y. G.; Chen, Y. C.; Zhou, J. H.; Wang, T.; Zhao, Y. G. *Solid State Commun.* **2009**, *149*, 585.
(11) Tian, L.; Zou, H. L.; Fu, J. X.; Yang, X. F.; Wang, Y.; Guo, H. L.; Fu, X. H.; Liang, C. L.; Wu, M. M.; Shen, P. K.; Gao, Q. M. *Adv. Funct. Mater.* **2010**, *20*, 617.
(12) Yang, J. H.; Hyodo, H.; Kimura, K.; Sasaki, T. *Nanotechnology* **2010**, *21*.
(13) Kanjwal, M. A.; Barakat, N. A. M.; Sheikh, F. A.; Khil, M. S.; Kim, H. Y. *J. Mate. Sci.* **2008**, *43*, 5489.
(14) Hu, L. H.; Sun, K. Q.; Peng, Q.; Xu, B. Q.; Li, Y. D. *Nano Res.* **2010**, *3*, 363.
(15) Xu, R.; Wang, J. W.; Li, Q. Y.; Sun, G. Y.; Wang, E. B.; Li, S. H.; Gu, J. M.; Ju, M. L. *J. Solid State Chem.* **2009**, *182*, 3177.
(16) Mei, W. M.; Huang, J.; Zhu, L. P.; Ye, Z. Z.; Mai, Y. J.; Tu, J. P. *J. Mater. Chem.* **2012**, *22*, 9315.
(17) Lou, X. W.; Deng, D.; Lee, J. Y.; Archer, L. A. *J. Mater. Chem.* **2008**, *18*, 4397.
(18) Xue, X. Y.; Yuan, S. A.; Xing, L. L.; Chen, Z. H.; He, B.; Chen, Y. J. *Chem .Commun.* **2011**, *47*, 4718.
(19) Lou, X. W.; Deng, D.; Lee, J. Y.; Feng, J.; Archer, L. A. *Adv. Mater.* **2008**, *20*, 258.
(20) Wang, R. M.; Liu, C. M.; Zhang, H. Z.; Chen, C. P.; Guo, L.; Xu, H. B.; Yang, S. H. *Appl. Phys. Lett.* **2004**, *85*, 2080.
(21) Zhan, F. M.; Geng, B. Y.; Guo, Y. J. *Chem.—Eur. J.* **2009**, *15*, 6169.
(22) Chen, L. F.; Hu, J. C.; Richards, R.; Prikhodko, S.; Kodambaka, S. *Nanoscale* **2010**, *2*, 1657.
(23) Dong, Q.; Su, H. L.; Song, F.; Zhang, D.; Wang, N. *J .Am. Ceram. Soc.* **2007**, *90*, 376.
(24) Fu, L.; Liu, Z. M.; Liu, Y. Q.; Han, B. X.; Hu, P. G.; Cao, L. C.; Zhu, D. B. *Adv. Mater.* **2005**, *17*, 217.
(25) Chen, J. S.; Zhu, T.; Hu, Q. H.; Gao, J. J.; Su, F. B.; Qiao, S. Z.; Lou, X. W. *ACS Appl. Mater. Inter.* **2010**, *2*, 3628.
(26) Yang, J.; Quaresma, S.; Mei, S.; Ferreira, J. M. F.; Norby, P. *Key Eng. Mater.* **2005**, *280*−*283*, 713.
(27) Ding, Y. S.; Xu, L. P.; Chen, C. H.; Shen, X. F.; Suib, S. L. *J. Phys. Chem. C* **2008**, *112*, 8177.
(28) Zhao, Z. G.; Geng, F. X.; Bai, J. B.; Cheng, H. M. *J. Phys. Chem. C* **2007**, *111*, 3848.
(29) Wang, Y.; Xia, H.; Lu, L.; Lin, J. Y. *ACS Nano* **2010**, *4*, 1425.
(30) Wang, X.; Yu, L. J.; Wu, X. L.; Yuan, F. L.; Guo, Y. G.; Ma, Y.; Yao, J. N. *J. Phys. Chem. C* **2009**, *113*, 15553.
(31) Li, C. C.; Yin, X. M.; Chen, L. B.; Li, Q. H.; Wang, T. H. *Appl. Phys. Lett.* **2010**, *97*.
(32) Wang, X.; Sumboja, A.; Khoo, E.; Yan, C. Y.; Lee, P. S. *J. Phys. Chem. C* **2012**, *116*, 4930.
(33) Shim, H. W.; Jin, Y. H.; Seo, S. D.; Lee, S. H.; Kim, D. W. *ACS Nano* **2011**, *5*, 443.
(34) Li, C. C.; Yin, X. M.; Li, Q. H.; Chen, L. B.; Wang, T. H. *Chem.—Eur. J.* **2011**, *17*, 1596.
(35) Du, N.; Zhang, H.; Chen, B.; Wu, J. B.; Ma, X. Y.; Liu, Z. H.; Zhang, Y. Q.; Yang, D.; Huang, X. H.; Tu, J. P. *Adv. Mater.* **2007**, *19*, 4505.
(36) Lee, K. H.; Song, S. W. *ACS Appl. Mater. Interfaces* **2011**, *3*, 3697.
(37) Jiang, J.; Liu, J. P.; Huang, X. T.; Li, Y. Y.; Ding, R. M.; Ji, X. X.; Hu, Y. Y.; Chi, Q. B.; Zhu, Z. H. *Cryst. Growth Des.* **2010**, *10*, 70.
(38) Wu, Z. S.; Ren, W. C.; Wen, L.; Gao, L. B.; Zhao, J. P.; Chen, Z. P.; Zhou, G. M.; Li, F.; Cheng, H. M. *Acs Nano* **2010**, *4*, 3187.
(39) Xiong, S. L.; Chen, J. S.; Lou, X. W.; Zeng, H. C. *Adv. Funct. Mater.* **2012**, *22*, 861.
(40) Wang, C.; Wang, D. L.; Wang, Q. M.; Wang, L. *Electrochim. Acta* **2010**, *55*, 6420.
(41) Xia, X. H.; Tu, J. P.; Xiang, J. Y.; Huang, X. H.; Wang, X. L.; Zhao, X. B. *J. Power Sources* **2010**, *195*, 2014.
(42) Xia, Y.; Zhang, W. K.; Xiao, Z.; Huang, H.; Zeng, H. J.; Chen, X. R.; Chen, F.; Gan, Y. P.; Tao, X. Y. *J. Mater. Chem.* **2012**, *22*, 9209.
(43) Liu, Y.; Mi, C. H.; Su, L. H.; Zhang, X. G. *Electrochim. Acta* **2008**, *53*, 2507.
(44) Hao, Q. Y.; Lei, D. N.; Yin, X. M.; Zhang, M.; Liu, S.; Li, Q. H.; Chen, L. B.; Wang, T. H. *J . Solid State Electrochem.* **2011**, *15*, 2563.